ACS Photonics

pubs.acs.org/journal/apchd5

Article

Cascaded Optical Nonlinearities in Dielectric Metasurfaces

Sylvain D. Gennaro, Chloe F. Doiron, Nicholas Karl, Prasad P. Iyer, Darwin K. Serkland, Michael B. Sinclair, and Igal Brener*

Cite This: *ACS Photonics* 2022, 9, 1026−1032

Read Online

ACCESS | Metrics & More | Article Recommendations | Supporting Information

ABSTRACT: Since the discovery of the laser, optical nonlinearities have been at the core of efficient light conversion sources. Typically, thick transparent crystals or quasi-phase matched waveguides are utilized in conjunction with phase-matching techniques to select a single parametric process. In recent years, due to the rapid developments in artificially structured materials, optical frequency mixing has been achieved at the nanoscale in subwavelength resonators arrayed as metasurfaces. Phase matching becomes relaxed for these wavelength-scale structures, and all allowed nonlinear processes can, in principle, occur on an equal footing. This could promote harmonic generation via a cascaded (consisting of several frequency mixing steps) process. However, so far, all reported work on dielectric metasurfaces have assumed frequency mixing from a direct (single step) nonlinear process. In this work, we prove the existence of cascaded second-order optical nonlinearities by analyzing the second- and third-wave mixing from a highly nonlinear metasurface in conjunction with polarization selection rules and crystal symmetries. We find that the third-wave mixing signal from a cascaded process can be of comparable strength to that from conventional third-harmonic generation and that surface nonlinearities are the dominant mechanism that contributes to cascaded second-order nonlinearities in our metasurface.

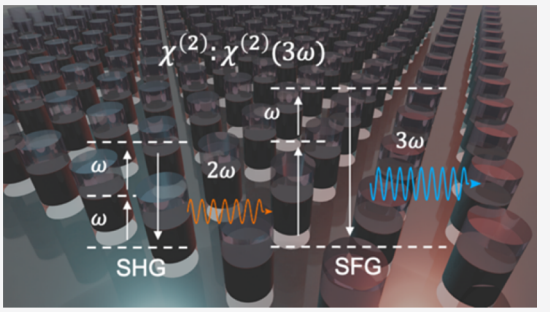

KEYWORDS: *metasurfaces, harmonic generation, cascaded optical nonlinearities, polarization*

In a nonlinear medium, harmonic generation at 3 times the pump frequency, ω, can be achieved by traditional third-harmonic generation (THG) from a direct $\chi^{(3)}$ process or via a $\chi^{(2)}$:$\chi^{(2)}$ cascaded process of second-harmonic generation (SHG) followed by sum frequency generation (SFG), as illustrated in Figure 1.[1−5] To distinguish this cascaded process from conventional THG, we denote the cascaded process as $\chi^{(2)}$:$\chi^{(2)}$ (3ω) and conventional THG as $\chi^{(3)}$:THG. Four-wave mixing, one of the hallmarks of third-order nonlinearities, can also be achieved by SHG of one pump beam, followed by difference frequency generation (DFG) with a second pump beam.[6] Traditionally, $\chi^{(2)}$:$\chi^{(2)}$ (3ω) is weak in bulk media since phase-matching limits frequency mixing to one process at a time.[7−9] In nonlinear metasurfaces, due to the relaxation of phase-matching limitations, several of the frequency mixing products observed experimentally might be explained by cascaded second-order optical nonlinearities.[10−17] However, given that both $\chi^{(3)}$:THG and $\chi^{(2)}$:$\chi^{(2)}$ (3ω) occur at the same frequencies and are assumed to have the same polarization response in cubic crystal systems,[18] it is difficult to distinguish between the two processes in these types of non-phase-matched systems. Understanding the origin of light conversion in these systems is critical since the efficiencies of cascaded harmonic generation could compete with those of conventional direct frequency mixing processes or even surpass them.[17,19]

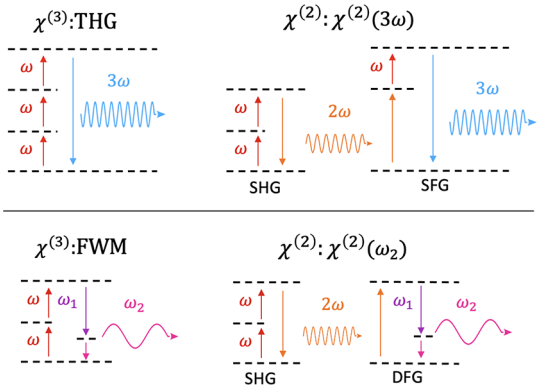

Figure 1. Cascaded vs direct frequency mixing processes. Schematic of harmonic generation of a wave at frequencies 3ω via direct $\chi^{(3)}$: THG $[\chi^{(3)}(-3\omega;\omega,\omega,\omega)]$ or through cascaded SHG and SFG. $[\chi^{(2)}(-2\omega;\omega,\omega):\chi^{(2)}(-3\omega;2\omega,\omega)]$; and at frequencies ω_2 via direct $\chi^{(3)}$:FWM $[\chi^{(3)}(-\omega_2;\omega_1,\omega,\omega)]$ or through cascaded SHG and DFG $[\chi^{(2)}(-2\omega;\omega,\omega):\chi^{(2)}(-\omega_2;\omega_1,2\omega)]$.

Received: December 16, 2021
Published: February 11, 2022

https://doi.org/10.1021/acsphotonics.1c01937
ACS Photonics 2022, 9, 1026−1032

In this work, we prove the existence of cascaded second-order optical nonlinearities by investigating second- and third-wave mixing from a dielectric metasurface made of GaAs nanocylinder resonators, isolated from a GaAs/AlGaAs substrate by an AlGaO spacer layer (see the Methods section for additional information on the fabrication process). The metasurface is illustrated in Figure 2a. We choose this design as it possesses a symmetric resonator geometry and the metasurface is known to exhibit intense harmonic emission at multiples of the pump frequency enhanced by the excitation of Mie-like optical resonant modes at the fundamental (i.e., pump) frequency (see Figure 2b).[20] The linear reflectance spectra shows a broad resonance with two distinct peaks characteristic of two Mie-like optical modes, namely, an electric dipole (ED) mode centered around 1200 nm and a magnetic dipole (MD) mode centered around 1400 nm.[14,20−23] Additional electric field data of the ED and MD modes are shown in Figure S1. At pump wavelengths resonant with the ED (1200 nm) and MD modes (1400 nm), the harmonic emissions at 2ω and 3ω are above the band gap of GaAs, and the substrate absorbs the radiated harmonics.

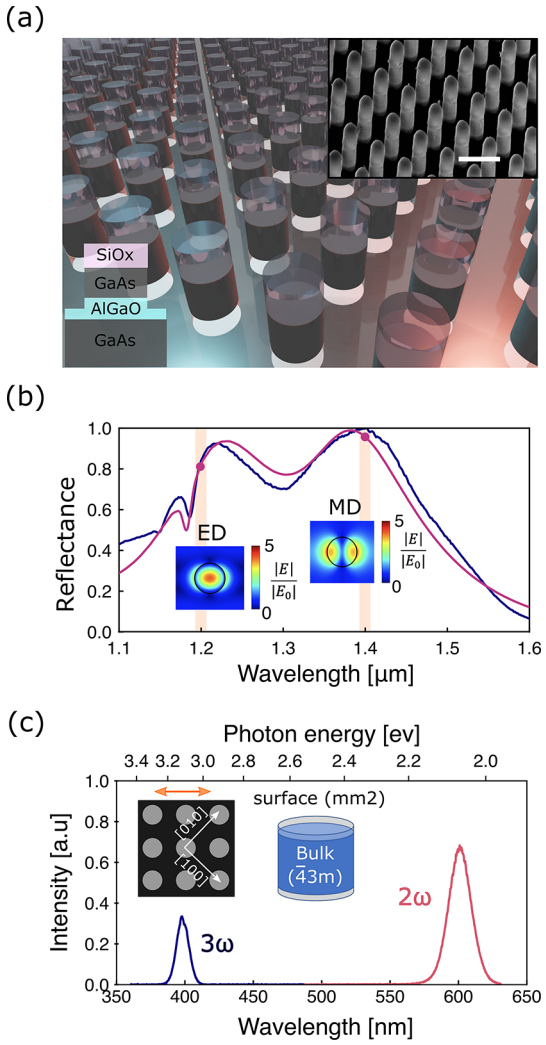

Figure 2. Optical modes and symmetry of our nonlinear metasurface. (a) Artistic representation of the dielectric metasurface considered in this work. Top inset is a tilted view of a scanning electron micrograph of the metasurface. White scale bar represents 1 μm. Bottom inset shows the different materials that constitutes each resonator. (b) Simulated (solid purple) and measured (solid blue) linear reflection spectra of our metasurface. Top views of normalized electric field distribution $|E|/|E_o|$ of the resonators are displayed for the ED mode at 1200 nm and the MD mode at 1400 nm. (c) Measured spectra of the nonlinear signal at 2ω (solid pink) and 3ω (solid blue) excited using a 1200 nm linearly polarized pump laser beam. Insets are a schematic of the metasurface showing the orientation of the GaAs crystal axes [100] and [010] as white arrows and the incident pump light polarization as a double orange arrow. The second schematic represents a GaAs nanocylinder where the crystal point-group symmetry of bulk ($\bar{4}3m$) and that of the top/bottom surface ($mm2$) are indicated.

Thus, we collect the harmonic emission using a reflection geometry. Our optical apparatus for the nonlinear measurements is described in the Methods section, and its schematic is presented in Figure S2. Examples of harmonic spectra at 2ω and 3ω are shown in Figure 2c for a pump wavelength of 1200 nm, with an incident peak irradiance of 2 GW/cm^2 and incident polarization parallel to the horizontal edge of our nanocylinder array, as illustrated by the orange double-sided arrows in the inset of Figure 2c. The crystal axes [100] and [010] of GaAs are at −45 and 45° with respect to the edge of our metasurface, respectively. Since the second- and third-order nonlinear susceptibility tensors are described in the principal axis frame of the crystal ([100], [010], and [001]), we perform the appropriate coordinate transformation when we subsequently model the nonlinear harmonic signal at 2ω and 3ω in Figure 3 (see Note S1).[23] Nonlinear optical modeling is carried out using a commercial finite-element solver including nonlinear optical tensors (see Supplementary Note 1). Polarization dependence modeling is then carried out self-consistently both at 2ω and 3ω.

In previous studies, a $\chi^{(2)}{:}\chi^{(2)}$ (3ω) process was isolated by rotating the sample in-plane and measuring the anisotropy of the total third-harmonic emission that arises from $\chi^{(2)}{:}\chi^{(2)}$ (3ω) interfering with $\chi^{(3)}$:THG.[19,24] Since the GaAs crystal belongs to the point-group symmetry $\bar{4}3m$, $\chi^{(3)}$:THG has a fourfold symmetry with respect to crystal orientation, as is commonly observed for cubic crystals.[19,24−26] We expect this to also be true for our metasurfaces due to the rotational symmetry of the nanocylinders and the fourfold symmetry of the cylinder array. However, in our measurements, we observe distinct deviations from a fourfold pattern, which we demonstrate to originate from a cascaded second-order process. To understand this cascaded process, we also investigate the symmetry of the optical fields at 2ω (SHG) and the second-order nonlinear susceptibility with respect to the crystal orientation.

Figure 3 shows the measured and simulated normalized intensities of the harmonic emissions at 2ω and 3ω as a function of incident polarization when optically pumping the ED mode at 1200 nm (Figure 3a,b), and the MD mode at 1400 nm (Figure 3c,d). We begin by discussing the nonlinear emission at 2ω (Figure 3a,c), where we observe a twofold symmetry in the measured total SH intensity with the maxima centered at 0 and 180° (relative to the axes of the nanocylinder array) for the ED mode and at 90 and 270° for the MD mode. However, the simulated SH considering only bulk second-order nonlinearities of GaAs ($\chi^{(2)}_{xzy} = \chi^{(2)}_{yzx} = \chi^{(2)}_{zxy} = 200$ [pm·V^{-1}] at ω and $\chi^{(2)}_{zxy} = 450$ [pm·V^{-1}] at 2ω)[27] predicts a fourfold symmetry of the SH emission (Figure 3b,d) with the minima for incident light polarized along the respective crystal axes [100] and [010] of GaAs as observed in the past literature.[22]

https://doi.org/10.1021/acsphotonics.1c01937
ACS Photonics 2022, 9, 1026−1032

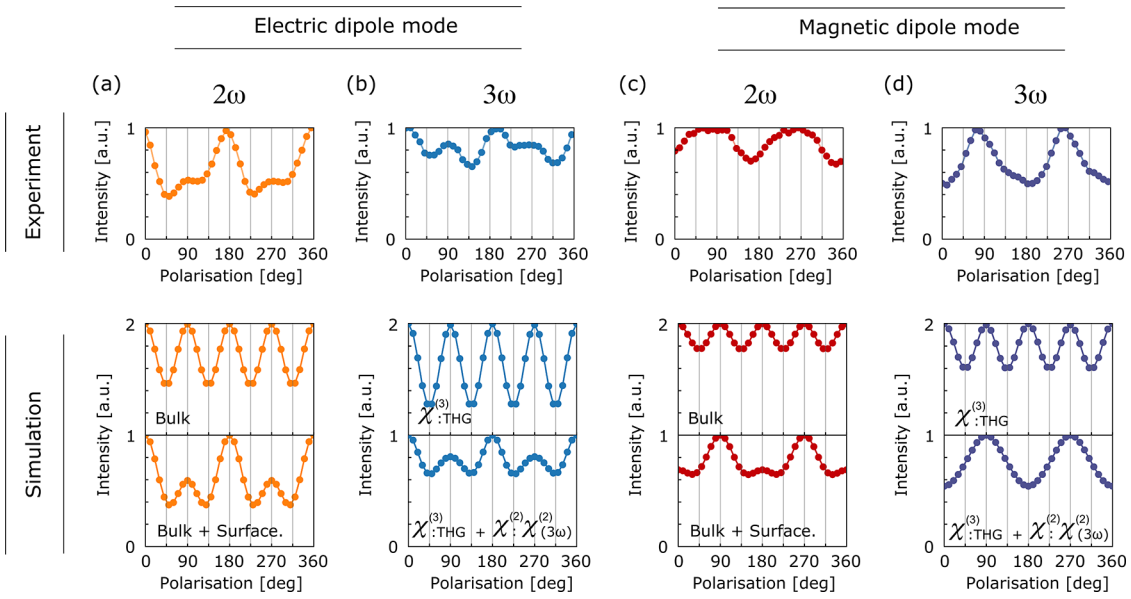

Figure 3. Identifying cascaded third harmonic with polarization selection rules and crystal symmetry. Measured (top panel) and simulated (middle and bottom panels) nonlinear harmonic intensities at (a,c) 2ω and (b,d), 3ω and for (a,b) ED mode excitation (λ = 1200 nm) and (c,d) MD mode excitation (λ = 1400 nm) while varying the polarization of the incident beam from 0 to 360°. Fourfold symmetry (middle panels) is characteristic of SHG from bulk nonlinearities and of THG via a direct third-order process ($\chi^{(3)}$:THG). Twofold symmetry indicates the presence of SHG from surface nonlinearities at 2ω and of third-wave mixing at 3ω via a cascaded second-order process. ($\chi^{(2)}$:$\chi^{(2)}(3\omega)$).

This fourfold symmetry is expected as the second-order nonlinear polarizability of bulk GaAs is non-zero only for cross terms, E_iE_j $\{i \neq j\}$ of the electric fields.[22]

The difference between the measured twofold and predicted fourfold symmetry cannot be explained using bulk second-order nonlinearities alone and suggests that surface nonlinearities must play a significant role in the total SH emission.[20,22,28−30] Indeed, it is well-known that the crystal symmetry of the surface of GaAs differs from that of the bulk: GaAs surfaces whose normal vectors are collinear to the principal crystal axes [100], [010], or [001] of GaAs belong to the point-group symmetry $mm2$.[26,31−33] While surface SHG generally appears as a weak anisotropy in the SHG symmetry studies of unstructured GaAs films,[31−33] dielectric metasurfaces magnify the effect of surface nonlinearities due to the larger total surface area and the strong electric field confinement inside the volume of each nanoscale resonator, which leads to greater electric field−surface interaction.[20,22,29]

Generally, it is challenging to model the resonator's surface nonlinearity on the sidewalls since the normal vector of the surface sidewalls varies with position and the symmetry of the nonlinear tensors are mostly known for surfaces whose normal vectors are aligned with the respective crystal axes of the families [100], [110], or [111].[26,29−32] From our experience, we also notice that during the dry etching process, the surface sidewalls are roughened, resulting in amorphous restructuring (see the Methods section). Thus, the surfaces are no longer crystalline facets with well-described local nonlinear polarizations. In contrast, the top and bottom surfaces of the GaAs resonators preserve their epitaxial growth crystallinity; hence, their orientation and symmetry remain well-defined. Therefore, we consider only the surface nonlinearities at the top and bottom surfaces. Recent studies on surface SHG in semiconductors considered regions on the order of a few nanometers at the material/air interface and demonstrated that this effective volume is a good representation of surface SHG.[28,29,34] Therefore, in our modeling, we consider two regions at the air/GaAs and GaAs/AlGaO interfaces with a thickness of 10 nm each and with a symmetry tensor of point-group symmetry $mm2$. When we include both surface and bulk nonlinearities, with the following surface-induced nonlinear coefficients: $\chi^{(2,s)}_{zxx} = \chi^{(2,s)}_{zyy} = 6\chi^{(2)}_{xzy}$, $\chi^{(2,s)}_{zzz} = 6\chi^{(2)}_{xzy}$, $\chi^{(2,s)}_{yxz} = \chi^{(2,s)}_{xzy} = 1.8\chi^{(2)}_{xzy}$, while maintaining the surface-induced nonlinear tensor symmetry (see Note S1), we successfully retrieve the twofold symmetry in the total SHG intensity (Figure 3a,c, bottom panels). Values of the surface nonlinearity coefficients were chosen to reproduce the twofold symmetry in the total SH intensity while respecting the symmetry constraints ($\chi^{(2,s)}_{zxx} = \chi^{(2,s)}_{zyy}$, $\chi^{(2,s)}_{zzz}$, $\chi^{(2,s)}_{yxz} = \chi^{(2,s)}_{xzy}$) imposed by the nonlinear tensor for [100] GaAs surfaces.[26] This result reaffirms the importance of surface-induced nonlinear effects in these types of nanophotonic systems.

We now discuss the polarization dependence of the harmonic emissions measured at 3ω. For both the ED and MD resonances, the measured symmetry of the 3ω emission (Figure 3b, d, top panels) deviates significantly from the fourfold symmetry expected from $\chi^{(3)}$:THG when considering bulk third-order nonlinearities alone; see Figure 3b,d middle panels. The $\chi^{(3)}(\omega)$, values found to reproduce our third harmonic experimental data: $\chi^{(3)}_{iiii} = 0.52 \times 10^{-19}$ [m^2·V^{-2}] and $\chi^{(3)}_{iijj} = 0.18 \times 10^{-19}$ [m^2·V^{-2}], are within ranges of predicted and measured values for THG.[3,35,36] We note here that surface-$\chi^{(3)}$ processes are negligible when compared to their dipole-allowed, bulk counterparts.[26] To explain this discrepancy in the polarization dependence, we include the cascaded $\chi^{(2)}$:$\chi^{(2)}$ (3ω) process and consider its interference with χ^3:THG (Figure 3b,d, bottom panels). Using this procedure, we can retrieve the twofold symmetry shown in our experiments. When pumping resonantly at the ED mode, the presence of $\chi^{(2)}$:$\chi^{(2)}$ (3ω) leads to an anisotropy in the total THG and seems to interfere destructively with $\chi^{(3)}$:THG in a similar fashion to past observations in bulk crystalline quartz.[19]

https://doi.org/10.1021/acsphotonics.1c01937
ACS Photonics 2022, 9, 1026−1032

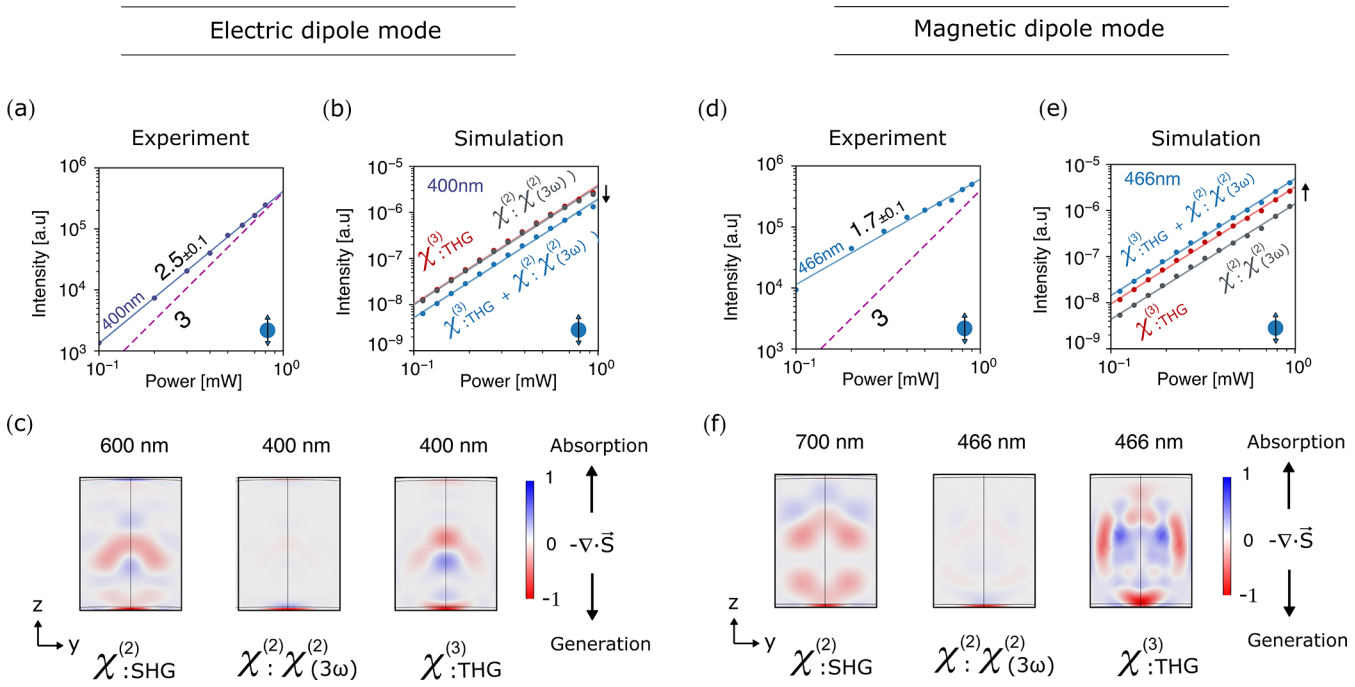

Figure 4. Origin of the cascaded third harmonic in dielectric metasurfaces. (a,d) Measured nonlinear signal at 3ω (solid dots) as a function of incident power plotted on a logarithmic scale for ED mode excitation at 1200 nm (3ω@400 nm) and MD mode excitation at 1400 nm (3ω@466 nm) with incident polarization at 90°. The numeric labels represent the exponent power coefficients, "a", of each nonlinear process obtained via a linear regression (solid line) on the logarithm of the data such that $\log_{10} P_{out} = a \log_{10} P_{in} + b$ assuming a power fluctuation of our laser of 4%. (b,e) Modeled nonlinear signal at 3ω (solid dots) for $\chi^{(3)}$:THG (solid red dots) and $\chi^{(2)}$:$\chi^{(2)}$(3ω) (solid gray dots) and the total 3ω signal (solid blue dots). For the ED mode, $\chi^{(2)}$:$\chi^{(2)}$(3ω) adds destructively with $\chi^{(3)}$:THG. For the MD mode, $\chi^{(2)}$:$\chi^{(2)}$(3ω) adds constructively with $\chi^{(3)}$:THG. Solid lines represent the respective linear fit for each harmonic process with predicted slopes of (b) 2.6 and (e) 2.5. (c) Divergence of the Poynting vector for $\chi^{(2)}$:SHG, $\chi^{(2)}$:$\chi^{(2)}$(3ω), and $\chi^{(3)}$:THG. Red and blue areas indicate where harmonic light is generated and dissipated, respectively.

For a pump resonant with the MD mode, however, the harmonic signal measured at ω shows a more distinct twofold symmetry. For completeness, we have also included in Figures S3 and S4 additional SHG and THG measured and simulated polarization data for some of the other incident wavelengths considered in this work. We find that our model can predict the overall trends of the nonlinear signal at 2ω for other pump wavelengths as the second-order nonlinear susceptibilities are relatively constant for the range of wavelengths at ω and 2ω considered in this work.[27] Since $\chi^{(3)}(\omega)$ values are predicted to vary more significantly over this spectral range, we may need to choose different values of $\chi^{(3)}(\omega)$ to obtain more accurate results for $\chi^{(3)}$:THG at other wavelengths.[3,35] In summary, any twofold symmetry in the harmonic emission at 3ω is a clear signature of a second-order cascaded process in our dielectric metasurface.

While characterizing the incident power dependencies of these harmonic processes (see Figure 4a, d), we find that the harmonic signal at 3ω scales sub-cubically for both the MD mode (≈1.7) and the ED mode (≈2.5). Figure S6 shows the power measurement of the nonlinear signal at 2ω. Sub-power scaling law is attributed in our system to the presence of competing nonlinear processes such as two-photon absorption (2PA) and the subsequent free carrier absorption in GaAs, as observed in our previous work.[20,37] Modeling this effect in our system (see Supplementary Note S2), we can retrieve sub-power scaling laws for both the signals at 2ω and 3ω, as shown in Figure 4b, e. While our simplified model predicts correctly the power scaling law for the ED (≈2.5), it underestimates the effect of 2PA for the MD mode given a reasonable 2PA coefficient for GaAs and field enhancement factors.

Using this self-consistent modeling that is representative of the physics of our metasurface, we can deduce the strength of each harmonic process. We find that when pumping at the ED mode, $\chi^{(2)}$:$\chi^{(2)}$ (3ω) can be of comparable strength to $\chi^{(3)}$:THG (Figure 4b) and adds destructively to $\chi^{(3)}$:THG such that the total nonlinear signal at 3ω is weakened. However, when pumping the MD mode, we find that $\chi^{(2)}$:$\chi^{(2)}$ (3ω) adds constructively to $\chi^{(3)}$:THG such that the total nonlinear signal at 3ω is strengthened (Figure 4e). Finally, Figure 4c, f shows the negative divergence of the Poynting vector, $-\nabla\cdot\vec{S}$, which indicates the locations where harmonic light is generated or dissipated. Integrating over the volumes of the resonator that we consider as representative of "bulk" and "surface" effects, we find that $\chi^{(2)}$:$\chi^{(2)}$ (3ω) is primarily generated via second-order nonlinearities at the surfaces.

The demonstration of cascaded optical nonlinearities in our dielectric metasurface suggests that alternative pathways to three-wave mixing, and more broadly high harmonic generation,[38,39] are achievable at the nanoscale, facilitated by the relaxation of phase matching. When designing and characterizing novel light conversion sources, it is paramount to account for all parasitic losses and unaccounted frequency mixing mechanisms. In this aspect, our work demonstrates an approach to isolate and characterize cascaded second-order optical nonlinearities, based on polarization selection rules and crystal symmetry, and quantify their effect on conventional direct harmonic generation. Our work also reaffirms the importance of considering surface nonlinearities in two-wave frequency mixing. Such an understanding and analysis could thus be used to significantly enhance efficiencies for frequency mixing processes as well as their quantum equivalent such as

https://doi.org/10.1021/acsphotonics.1c01937
ACS Photonics 2022, 9, 1026−1032

spontaneous parametric downconversion and thereby pave the way for a plethora of novel compact light conversion sources based on cascaded second-order optical nonlinearities.

METHODS

Simulated Reflectance Spectra. The reflectance spectra of the metasurface were simulated using the finite difference time-domain method (Lumerical Inc.) under plane wave excitation with periodic boundary conditions. The structure consists of an array of GaAs/AlGaO nanocylinders with a diameter of 350 nm, a periodicity of 750 nm, and a total height of 900 nm. The height of the nanocylinder is partitioned into a 300 nm SiO_x etch mask cap (top), a 450 nm GaAs layer (middle), and a 150 nm AlGaO layer (bottom). The nanocylinder rests on an estimated 250 nm unetched AlGaO oxide layer on top of a GaAs [001] substrate. The GaAs and SiO_x refractive index values were taken from the database of the finite difference time-domain software. AlGaO was modeled as a nondispersive medium with a refractive index of $n = 1.6$. Additional features such as the reflectance dip observed around 1170 nm arise from off-normal incidence excitation due to the finite numerical aperture of our optical system. This was modeled in simulation as a plane wave tilted by 2.5°. Off normal incidence can excite higher-order nonradiative modes.

Reflectance Spectroscopy. The linear reflectance spectra of the metasurface were measured using two home-built white-light spectroscopy setups. The near-infrared measurement spectra from 900 to 1600 nm were measured by focusing the broadband white light from a stabilized tungsten−halogen lamp onto the sample with a 50 mm plano-convex lens. In reflection, the scattering is collected by the same lens and directed into an InGaAs Peltier-cooled spectrometer. Each reflection spectrum is normalized using the reflectance of a gold mirror as a reference measured under the same experimental condition. For the visible regime (400−900 nm), the incoherent light from a thermal white light source is focused onto our sample with a microscope objective (5×, NA = 0.13). We reduce the back aperture with an iris to limit the range of incidence angles. The light is then redirected onto the entrance slit of a spectrometer. Each reflection spectrum of the metasurface is normalized using the reflectance of a silver mirror as a reference measured under the same experimental condition.

Sample Fabrication. The dielectric resonators are fabricated using standard electron-beam lithography and inductively coupled plasma (ICP) dry etch. The sample is grown using molecular beam epitaxy. We start with a GaAs substrate of crystal orientation [001] at the bottom, and then, three alternating layers of 400 nm thick $Al_{0.85}Ga_{0.15}As$ and 450 nm thick GaAs [001] are grown successively on the top (wafer VA0729). For this work, we will only use the top two layers to make the resonators. We then spin-coat a negative-tone hydrogen silsesquioxane (HSQ Fox-16) electron beam resist. Circular disk patterns are written using a 100 keV electron beam that converts the area of exposed HSQ to SiO_x. The unexposed resist is developed using tetramethylammonium hydroxide (TMAH), leaving ∼300 nm tall SiO_x nanodisks as hard etch masks. We then transfer the pattern onto the GaAs and AlGaAs layers using a chlorine-based (both Cl_2 and BCl_3) ICP etch. We stop the etch when the AlGaAs layer is etched to half of its depth. Finally, the sample was placed in a tube furnace at ∼420 °C for a selective wet oxidization process that converts $Al_{0.85}Ga_{0.15}As$ into its oxide $(Al_xGa_{1-x})_2O_3$, which has a refractive index of $n \approx 1.6$. Note that the oxide has a larger lattice constant than AlGaAs, which can cause the oxide layer to expand and be slightly larger than 400 nm.

Nonlinear Characterization. The metasurface is pumped by nominal <80 fs optical pulses at a 1 MHz repetition rate with the wavelength ranging from 1100 to 1600 nm. See Figure S1 for a schematic of the apparatus. The output power is controlled by a pair of a Glan−Taylor polarizer and an achromatic half-wave plate. Three long-pass filters with respective cutoff wavelengths of 830, 980, and 1064 nm reject any low frequency emission from the laser. Then, the pump beam is redirected onto the back aperture of a microscope lens (20×, NA = 0.45) with a 90:10 (T/R) beam splitter. We place an iris in the beam path to reduce the beam spot diameter from 6 to 1 mm, which corresponds to an effective NA of 0.077. Since most of the generated harmonic waves have photon energies above the GaAs band gap and thus would be absorbed by the GaAs substrate in transmission, we collect harmonic light in reflection by the same objective. The harmonic signal is then redirected using a multimode fiber onto the entrance slit of a spectrometer connected to a Peltier-cooled CCD camera. To control the incident polarization, we place an achromatic 690−1200 nm half-wave plate in front of the microscope objective. We verify that our optics are polarization insensitive for both the fundamental and harmonic wavelengths and performed consecutive measurements to eliminate laser power fluctuations. We note that, in our experiment, our nanocylinders are rotationally symmetric along their main axes and the linear permittivity of GaAs is isotropic. Therefore, rotating the incident pump polarization at normal incidence is equivalent to rotating the crystal axes (see Figure S3).

Nonlinear Simulation. Nonlinear simulations are performed using the commercial software COMSOL in the frequency domain using the wave-optic module. First, we calculate the linear electric field at the fundamental frequency and then calculate the respective nonlinear polarizabilities of each process as nonlinear sources. We then extract the average Poynting vector emitted at these nonlinear frequencies from the metasurface. In cubic crystal systems of point-group symmetry $\bar{4}3m$, the third-order susceptibility tensor of GaAs has only two independent elements $\chi^{(3)}_{xxxx}$ and $\chi^{(3)}_{xxyy}$ such that the nonlinear polarization of $\chi^{(3)}$:THG can be expressed in the principal-axis coordinate of the crystal, i, [100], j, [010], and k, [001] as $P_i = \epsilon_0[3\chi^{(3)}_{xxyy}E_i(\omega)(E\cdot E) + (\chi^{(3)}_{xxxx} - 3\chi^{(3)}_{xxyy})E_i(\omega)^3$, $i \in \{x, y, z\}$,[26] where ϵ_0 is the vacuum permittivity and E_i and E are the electric field components at the pump frequency, ω. To model $\chi^{(2)}$:$\chi^{(2)}$ (3ω), we first model SHG using second-order susceptibility's values of bulk GaAs and estimate values for surface SHG from our model. Then, we model SFG using the calculated fundamental and SHG field and the same partition bulk/surface of our nanocylinder. In the principal-axis system of the crystal {[100], [010], [001]}, the second-order bulk nonlinear susceptibility has only three nonvanishing, equal tensor components, $\chi^{(2)}_{ijk} = \chi^{(2)}_{jki} = \chi^{(2)}_{kij}$, where $\{i, j, k\} \in \{x, y, z\}$ such that the nonlinear polarization of SHG in the contracted notation matrix form is given by $P_i(2\omega) = 4\epsilon_0 d_{14}E_kE_j$ and the nonlinear polarization of SFG in the contracted notation matrix form is given by $P_i(2\omega) = 4\epsilon_0 d_{14}[E_j(\omega_1)E_k(\omega_2) + E_k(\omega_1)E_j(\omega_2)]$. For the top and bottom surfaces of GaAs, the crystal symmetry at the surface leads us to the following relations for the second-order susceptibility. $P^{(2)}_x = 4\epsilon_0 d^s_{15}E_zE_x$, $P^{(2)}_y = 4\epsilon_0 d^s_{24}E_zE_y$, and $P^{(2)}_z = 4\epsilon_0[d^s_{31}E^2_x + d^s_{32}E^2_y + d^s_{33}E^2_z]$. Since

https://doi.org/10.1021/acsphotonics.1c01937
ACS Photonics 2022, 9, 1026−1032

the orientation of the array is at 45° with the respective crystal axes, we have expressed the nonlinear polarizability in the laboratory frame using Euler rotation matrices. The full expression of the second- and third-order nonlinear polarizabilities used in our full-wave simulation are given in Supplementary Note S1. We also perform any additional simulations with different coefficient values of the third-order nonlinear tensors while respecting the symmetry constraint imposed to confirm the fourfold symmetry character of $\chi^{(3)}$:THG.

■ ASSOCIATED CONTENT

Supporting Information

The Supporting Information is available free of charge at https://pubs.acs.org/doi/10.1021/acsphotonics.1c01937.

Additional information on fabrication, optical apparatus, and linear and nonlinear modeling (PDF)

■ AUTHOR INFORMATION

Corresponding Author

Igal Brener − *Sandia National Laboratories, Albuquerque, New Mexico 87185, United States; Center for Integrated Nanotechnologies, Sandia National Laboratories, Albuquerque, New Mexico 87123, United States;* orcid.org/0000-0002-2139-5182; Email: ibrener@sandia.gov

Authors

Sylvain D. Gennaro − *Sandia National Laboratories, Albuquerque, New Mexico 87185, United States; Center for Integrated Nanotechnologies, Sandia National Laboratories, Albuquerque, New Mexico 87123, United States;* orcid.org/0000-0002-2209-0831

Chloe F. Doiron − *Sandia National Laboratories, Albuquerque, New Mexico 87185, United States; Center for Integrated Nanotechnologies, Sandia National Laboratories, Albuquerque, New Mexico 87123, United States*

Nicholas Karl − *Sandia National Laboratories, Albuquerque, New Mexico 87185, United States; Center for Integrated Nanotechnologies, Sandia National Laboratories, Albuquerque, New Mexico 87123, United States;* orcid.org/0000-0001-8478-7856

Prasad P. Iyer − *Sandia National Laboratories, Albuquerque, New Mexico 87185, United States; Center for Integrated Nanotechnologies, Sandia National Laboratories, Albuquerque, New Mexico 87123, United States*

Darwin K. Serkland − *Sandia National Laboratories, Albuquerque, New Mexico 87185, United States*

Michael B. Sinclair − *Sandia National Laboratories, Albuquerque, New Mexico 87185, United States*

Complete contact information is available at: https://pubs.acs.org/10.1021/acsphotonics.1c01937

Author Contributions

S.D.G. and I.B. designed the study, S.D.G. simulated the linear response, D.K.S. fabricated the sample, S.D.G. and P.P.I. measured the linear spectra, S.D.G. characterized the nonlinear response, S.D.G., C.D., and N.K. developed the nonlinear numerical model. S.D.G. wrote the manuscript with inputs from all authors.

Funding

U.S. Department of Energy (BES 20-017574).

Notes

The authors declare no competing financial interest.

■ ACKNOWLEDGMENTS

This work was supported by the U.S. Department of Energy, Office of Basic Energy Sciences, Division of Materials Sciences and Engineering and performed, in part, at the Center for Integrated Nanotechnologies, an Office of Science User Facility operated for the U.S. Department of Energy (DOE) Office of Science. Sandia National Laboratories is a multimission laboratory managed and operated by National Technology and Engineering Solutions of Sandia, LLC, a wholly owned subsidiary of Honeywell International, Inc., for the U.S. Department of Energy's National Nuclear Security Administration under contract DE-NA0003525. This paper describes objective technical results and analysis. Any subjective views or opinions that might be expressed in the paper do not necessarily represent the views of the U.S. Department of Energy or the United States Government.

■ REFERENCES

(1) Khurgin, J. B.; Obeidat, A.; Lee, S. J.; Ding, Y. J. Cascaded Optical Nonlinearities: Microscopic Understanding as a Collective Effect. *J. Opt. Soc. Am. B* **1997**, *14*, 1977−1983.

(2) Bosshard, C.; Gubler, U.; Kaatz, P.; Mazerant, W.; Meier, U. Non-Phase-Matched Optical Third-Harmonic Generation in Noncentrosymmetric Media: Cascaded Second-Order Contributions for the Calibration of Third-Order Nonlinearities. *Phys. Rev. B: Condens. Matter Mater. Phys.* **2000**, *61*, 10688−10701.

(3) Yablonovitch, E.; Flytzanis, C.; Bloembergen, N. Anisotropic Interference of Three-Wave and Double Two-Wave Frequency Mixing in GaAs. *Phys. Rev. Lett.* **1972**, *29*, 865−868.

(4) Stegeman, G. I.; Hagan, D. J.; Torner, L. $\chi(2)$ Cascading Phenomena and Their Applications to All-Optical Signal Processing, Mode-Locking, Pulse Compression and Solitons. *Opt. Quantum Electron.* **1996**, *28*, 1691−1740.

(5) Stegeman, G. I. $\chi(2)$ Cascading: Nonlinear Phase Shifts. *Quantum Semiclassical Opt.* **1997**, *9*, 139−153.

(6) Chou, M. H.; Parameswaran, K. R.; Fejer, M. M.; Brener, I. Multiple-Channel Wavelength Conversion by Use of Engineered Quasi-Phase-Matching Structures in LiNbO_3 Waveguides. *Opt. Lett.* **1999**, *24*, 1157−1159.

(7) Chou, M. H.; Brener, I.; Fejer, M. M.; Chaban, E. E.; Christman, S. B. 1.5-μm-Band Wavelength Conversion Based on Cascaded Second-Order Nonlinearity in $LiNBO_3$ waveguides. *IEEE Photonics Technol. Lett.* **1999**, *11*, 653−655.

(8) Becouarn, L.; Lallier, E.; Brevignon, M.; Lehoux, J. Cascaded Second-Harmonic and Sum-Frequency Generation of a CO_2 Laser by Use of a Single Quasi-Phase-Matched GaAs Crystal. *Opt. Lett.* **1998**, *23*, 1508−1510.

(9) Qi, H.; Wang, Z.; Yu, F.; Sun, X.; Xu, X.; Zhao, X. Cascaded Third-Harmonic Generation with One KDP Crystal. *Opt. Lett.* **2016**, *41*, 5823−5826.

(10) Rahmani, M.; Leo, G.; Leo, G.; Brener, I. Nonlinear Frequency Conversion in Optical Nanoantennas and Metasurfaces: Materials Evolution and Fabrication. *Opto-Electron. Adv.* **2018**, *1*, 18002101−18002112.

(11) Gennaro, S. D.; Li, Y.; Maier, S. A.; Oulton, R. F. Nonlinear Pancharatnam−Berry Phase Metasurfaces beyond the Dipole Approximation. *ACS Photonics* **2019**, *6*, 2335−2341.

(12) Koshelev, K.; Kruk, S.; Melik-Gaykazyan, E.; Choi, J.-H.; Bogdanov, A.; Park, H.-G.; Kivshar, Y. Subwavelength Dielectric Resonators for Nonlinear Nanophotonics. *Science* **2020**, *367*, 288−292.

(13) Krasnok, A.; Tymchenko, M.; Alù, A. Nonlinear Metasurfaces: A Paradigm Shift in Nonlinear Optics. *Mater. Today* **2018**, *21*, 8−21.

(14) Liu, S.; Vabishchevich, P. P.; Vaskin, A.; Reno, J. L.; Keeler, G. A.; Sinclair, M. B.; Staude, I.; Brener, I. An All-Dielectric Metasurface as a Broadband Optical Frequency Mixer. *Nat. Commun.* **2018**, *9*, 2507.
(15) Gennaro, S. D.; Li, Y.; Maier, S. A.; Oulton, R. F. Double Blind Ultrafast Pulse Characterization by Mixed Frequency Generation in a Gold Antenna. *ACS Photonics* **2018**, *5*, 3166−3171.
(16) Carletti, L.; Kruk, S. S.; Bogdanov, A. A.; De Angelis, C.; Kivshar, Y. High-Harmonic Generation at the Nanoscale Boosted by Bound States in the Continuum. *Phys. Rev. Res.* **2019**, *1*, 023016.
(17) Celebrano, M.; Locatelli, A.; Ghirardini, L.; Pellegrini, G.; Biagioni, P.; Zilli, A.; Wu, X.; Grossmann, S.; Carletti, L.; De Angelis, C.; Duò, L.; Hecht, B.; Finazzi, M. Evidence of Cascaded Third-Harmonic Generation in Noncentrosymmetric Gold Nanoantennas. *Nano Lett.* **2019**, *19*, 7013−7020.
(18) Zilli, A.; Rocco, D.; Finazzi, M.; Di Francescantonio, A.; Duò, L.; Gigli, C.; Marino, G.; Leo, G.; De Angelis, C.; Celebrano, M.; Di Francescantonio, A.; Duò, L.; Gigli, C.; Marino, G.; Leo, G.; De Angelis, C.; Celebrano, M. Frequency Tripling via Sum-Frequency Generation at the Nanoscale. *ACS Photonics* **2021**, *8*, 1175−1182.
(19) Meredith, G. R. Cascading in Optical Third-Harmonic Generation by Crystalline Quartz. *Phys. Rev. B: Condens. Matter Mater. Phys.* **1981**, *24*, 5522−5532.
(20) Liu, S.; Sinclair, M. B.; Saravi, S.; Keeler, G. A.; Yang, Y.; Reno, J.; Peake, G. M.; Setzpfandt, F.; Staude, I.; Pertsch, T.; Brener, I. Resonantly Enhanced Second-Harmonic Generation Using III-V Semiconductor All-Dielectric Metasurfaces. *Nano Lett.* **2016**, *16*, 5426−5432.
(21) Carletti, L.; Locatelli, A.; Stepanenko, O.; Leo, G.; De Angelis, C. Enhanced Second-Harmonic Generation from Magnetic Resonance in AlGaAs Nanoantennas. *Opt. Express* **2015**, *23*, 26544.
(22) Löchner, F. J. F.; Fedotova, A. N.; Liu, S.; Keeler, G. A.; Peake, G. M.; Saravi, S.; Shcherbakov, M. R.; Burger, S.; Fedyanin, A. A.; Brener, I.; Pertsch, T.; Setzpfandt, F.; Staude, I. Polarization-Dependent Second Harmonic Diffraction from Resonant GaAs Metasurfaces. *ACS Photonics* **2018**, *5*, 1786−1793.
(23) Camacho-Morales, R.; Rahmani, M.; Kruk, S.; Wang, L.; Xu, L.; Smirnova, D. A.; Solntsev, A. S.; Miroshnichenko, A.; Tan, H. H.; Karouta, F.; Naureen, S.; Vora, K.; Carletti, L.; De Angelis, C.; Jagadish, C.; Kivshar, Y. S.; Neshev, D. N. Nonlinear Generation of Vector Beams from AlGaAs Nanoantennas. *Nano Lett.* **2016**, *16*, 7191−7197.
(24) Petrocelli, G.; Pichini, E.; Scudieri, F.; Martellucci, S. Anisotropic Effects in the Third-Harmonic-Generation Process in Cubic Crystals. *J. Opt. Soc. Am. B* **1993**, *10*, 918.
(25) Lüpke, G.; Marowsky, G. Third-Order Processes and Their Relation to Structural Symmetry. *Appl. Phys. B: Photophys. Laser Chem.* **1991**, *53*, 71−81.
(26) Sipe, J.; Moss, D.; van Driel, H. Phenomenological Theory of Optical Second- and Third-Harmonic Generation from Cubic Centrosymmetric Crystals. *Phys. Rev. B: Condens. Matter Mater. Phys.* **1987**, *35*, 1129−1141.
(27) Bergfeld, S.; Daum, W. Second-Harmonic Generation in GaAs: Experiment versus Theoretical Predictions of $\chi(2)$Xyz. *Phys. Rev. Lett.* **2003**, *90*, 036801.
(28) Sanatinia, R.; Anand, S.; Swillo, M. Experimental Quantification of Surface Optical Nonlinearity in GaP Nanopillar Waveguides. *Opt. Express* **2015**, *23*, 756−764.
(29) Timbrell, D.; You, J. W.; Kivshar, Y. S.; Panoiu, N. C. A Comparative Analysis of Surface and Bulk Contributions to Second-Harmonic Generation in Centrosymmetric Nanoparticles. *Sci. Rep.* **2018**, *8*, 3586.
(30) Pakhomov, A. V.; Löchner, F. J. F.; Zschiedrich, L.; Saravi, S.; Hammerschmidt, M.; Burger, S.; Pertsch, T.; Setzpfandt, F. Far-Field Polarization Signatures of Surface Optical Nonlinearity in Non-centrosymmetric Semiconductors. *Sci. Rep.* **2020**, *10*, 10545.
(31) Yamada, C.; Kimura, T. Anisotropy in Second-Harmonic Generation from Reconstructed Surfaces of GaAs. *Phys. Rev. Lett.* **1993**, *70*, 2344−2347.
(32) Yamada, C.; Kimura, T. Rotational Symmetry of the Surface Second-Harmonic Generation of Zinc-Blende-Type Crystals. *Phys. Rev. B: Condens. Matter Mater. Phys.* **1994**, *49*, 14372−14381.
(33) Armstrong, S. R.; Hoare, R. D.; Pemble, M. E.; Povey, I. M.; Stafford, A.; Taylor, A. G. Optical Second Harmonic Generation Studies of the Nature of the GaAs(100) Surface in Air. *J. Cryst. Growth* **1992**, *120*, 94−97.
(34) Javůrek, D.; Peřina, J. Analytical Model of Surface Second-Harmonic Generation. *Sci. Rep.* **2019**, *9*, 4679.
(35) Ching, W. Y.; Huang, M.-Z. Calculation of Optical Excitations in Cubic Semiconductors. III. Third-Harmonic Generation. *Phys. Rev. B: Condens. Matter Mater. Phys.* **1993**, *47*, 9479−9491.
(36) Moss, D. J.; Ghahramani, E.; Sipe, J. E.; van Driel, H. M. Band-Structure Calculation of Dispersion and Anisotropy in $\chi(3)$ for Third-Harmonic Generation in Si, Ge, and GaAs. *Phys. Rev. B: Condens. Matter Mater. Phys.* **1990**, *41*, 1542−1560.
(37) Karl, N.; Vabishchevich, P. P.; Shcherbakov, M. R.; Liu, S.; Sinclair, M. B.; Shvets, G.; Brener, I. Frequency Conversion in a Time-Variant Dielectric Metasurface. *Nano Lett.* **2020**, *20*, 7052−7058.
(38) Yang, Y.; Lu, J.; Manjavacas, A.; Luk, T. S.; Liu, H.; Kelley, K.; Maria, J.-P.; Runnerstrom, E. L.; Sinclair, M. B.; Ghimire, S.; Brener, I. High-Harmonic Generation from an Epsilon-near-Zero Material. *Nat. Phys.* **2019**, *15*, 1022−1026.
(39) Ghimire, S.; Reis, D. A. High-Harmonic Generation from Solids. *Nat. Phys.* **2019**, *15*, 10−16.

https://doi.org/10.1021/acsphotonics.1c01937
ACS Photonics 2022, 9, 1026−1032